Monitored reconstruction improved by post-processing neural network

A.V. Yamaev [1,2]
[1] Moscow State University, Russia, 119991, Moscow, Leninskie Gory, 1;
[2] Smart Engines Service LLC, Russia, Moscow,
119234, Moscow, Russia, 60th Anniversary of October Avenue 9

Abstract

Computed tomography (CT) is widely utilized for analyzing internal structures, but the limitations of traditional reconstruction algorithms, which often require a large number of projections, restrict their effectiveness in time-critical tasks or for biological objects studying. Recently Monitored reconstruction approach was proposed for reducing the requirement of dose load. In this paper, there were investigated the advantages of using post-processing neural networks within a monitored reconstruction approach. Three algorithms, namely FBP, FBPConvNet, and LRFR, are evaluated based on their mean count of projections required for the achievement of target reconstruction accuracy. A novel training method specifically designed for neural network algorithms within the Monitored reconstruction framework is proposed. It is shown that the use of the LRFR approach allows one to achieve both a reduction in the number of measured projections and an improvement in the reconstruction accuracy over a certain range of stopping rules. These findings highlight the significant potential of neural networks to be used in the Monitored reconstruction approach.

Keywords: monitored reconstruction, few-view, computed tomography, x-ray, deep learning, post-processing neural network.

Introduction

Computed tomography (CT) is a widely used medical imaging technique that provides detailed cross-sectional images of the internal structures of the human body. It plays a crucial role in the diagnosis, treatment planning, and monitoring of various medical conditions. CT scans are acquired by rotating an X-ray source and detector around the patient, capturing a series of X-ray projections from different angles. These projections are then mathematically reconstructed into a 3D image using specialized algorithms.

Traditional CT reconstruction algorithms, such as filtered back projection (FBP) [31], have been the gold standard for many years. These algorithms assume ideal imaging conditions and make simplifying assumptions about the X-ray acquisition process. However, in practice, CT imaging is often subject to limitations such as limited data [3, 4, 5, 6], noise [7, 8, 9, 10], and more [11, 12, 13, 14]. These factors can significantly degrade the quality of reconstructed images, making accurate diagnosis and interpretation challenging.

In recent years, there has been a growing interest in applying neural networks to improve the reconstruction quality in CT imaging. Neural network-based algorithms leverage the power of deep learning models to learn complex mappings between the acquired data and the desired high-quality images. These models have demonstrated remarkable success in various image processing tasks, including image denoising [15], super-resolution [16], and inpainting [17]. By leveraging the representational learning capabilities of neural networks, CT reconstruction algorithms can effectively compensate for the limitations of traditional methods and produce high-quality images from limited [18] or noisy data [19].

However, one significant challenge in CT reconstruction revolves around the inherent trade-off between reconstruction quality and considerations such as dose absorption and projection measure time. Traditional algorithms, while capable of delivering high-quality results, often demand a large number of projections, leading to increased dose absorption by the patient [10] or prolonged experimental durations. The two most widely used methods of dose reduction are: lowering the applied dose for one projection (by reducing the exposure time, X-ray tube voltage, etc.) and reducing the number of projections to be measured. The first method leads to increased noise in the projections and the second to linear artifacts in the reconstruction image. Usually, the number of projections is reduced to a fixed number regardless of the object structure. However, the authors in [1] showed that there is a more optimal scanning scheme called "monitored reconstruction". This approach views CT experiments as "anytime" algorithms, allowing them to be stopped when a predetermined stop rule is satisfied. The authors propose a new paradigm for CT experimentation, where projections are collected iteratively, and the reconstruction process is halted when the trade-off between reconstruction quality and projection measure cost reaches near-optimal levels. Remarkably, this approach demonstrates a remarkable ability to minimize X-ray absorption and experiment time while preserving reconstruction quality to a great extent.

On the other hand, neural network-based approaches have demonstrated the potential to achieve superior reconstruction quality compared to the reconstruction algorithms used in [1]. Numerous papers have proposed neural network solutions to address the issue of a limited number of projection angles. These methods can generally be categorized into three groups:

1. Postprocessing methods: These techniques enhance the quality of reconstructed images without requiring access to the projections. [22]

2. Preprocessing methods: These approaches process projections before applying the reconstruction algorithm. [20]

3. Neural network reconstructors: These algorithms take the projections as input and produce a reconstruction image as output. [21]

While all the mentioned methods can significantly enhance the quality of reconstruction within the specific dataset they were trained on, postprocessing networks are currently the closest to real-world applications.

To address this challenge, we propose a Neural monitored reconstruction approach improved by a post-processing neural network for CT reconstruction. The key idea is to combine a monitored reconstruction approach with algorithms of neural network reconstruction. The new approach provides an early stopping mechanism based on the confidence of the neural network predictions and a balance between reconstruction speed, quality, and dose absorbed by the patient.

In this study, we aim to investigate the effectiveness of our anytime reconstruction approach compared to traditional algorithms and existing neural network-based methods. We will evaluate the reconstruction quality by projection count through experiments on the CT dataset "Low Dose CT Grand Challenge" [2]. This dataset was specifically designed to test neural network reconstructive algorithms in the presence of noise in the projections. It contains high-dose reconstruction images and the results of this study have the potential to significantly advance the field of CT imaging by providing improved reconstruction capabilities that can be tailored to specific clinical requirements.

The structure of the article is presented as follows. Section 2 contains a description of the monitored reconstruction approach. Section 3 contains a description of the proposed approach for combining neural network reconstruction and monitored reconstruction. Section 4 includes the results of the conducted experiments and comparisons. Section 5 contains a condemnation of the results obtained and the shortcomings of the proposed approach, as well as ideas for further research. Section 6 contains the conclusion.

1. Monitored reconstruction

Fig. 1 contains FBP reconstruction images by varying counts of projections simulated from high-dose reconstructions from Low Dose CT Grand Challenge. High dose reconstruction was ground truth in Fig. 1. Fig. 3 shows the dependence between mean squared error (MSE) to measured projection count for 25 random objects from the Low Dose CT Grand Challenge dataset at different numbers of measured projections which also simulated (see section 2 for detailed experiment description). As can be seen in Fig. 2 and Fig. 3, for each fixed number of measured projections, the reconstruction error varies widely from object to object. Assume we require a reconstruction MSE of 0.01 for subsequent analysis. In an always-fixed number of projections to be measured, we would need to collect 107 projections per experiment to achieve the desired accuracy in only 90 percent of the experiments shown in Fig. 3. If we were able to stop the measurement process just at the moment of achieving the desired accuracy of the reconstruction, we would collect on average only 66 projections.
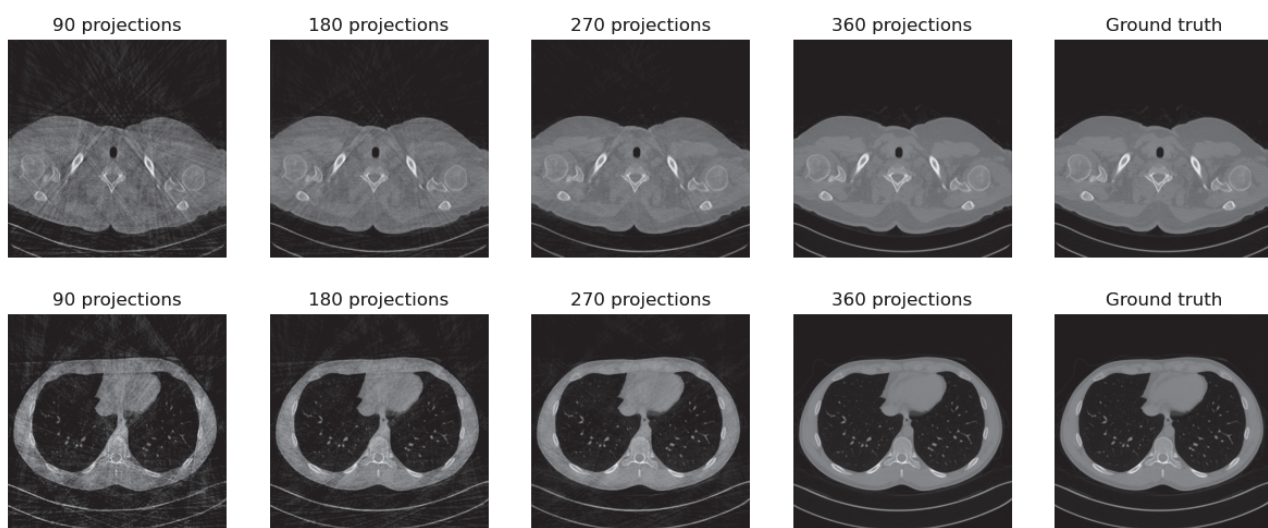

Fig. 1. Partial reconstruction images were created by the FBP algorithm from different counts of measured projections
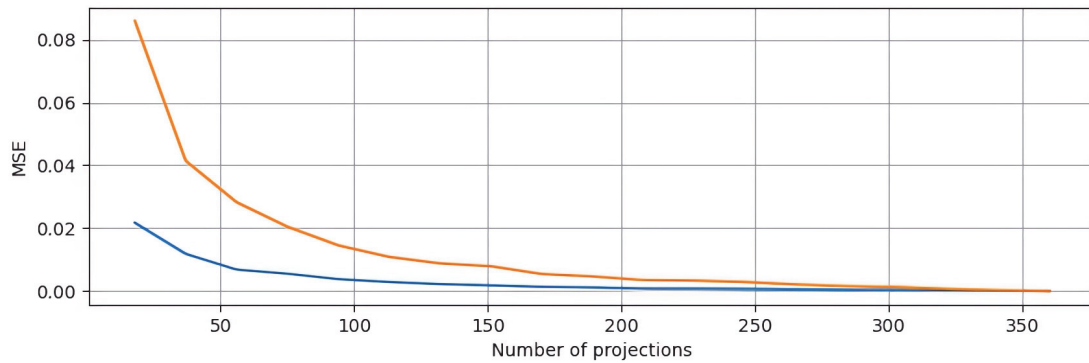
Fig. 2. Graph of relationship between the number of measured projections and the mean-square error between the reconstructed images and ideal reconstructions for two objects shown in Fig. 1
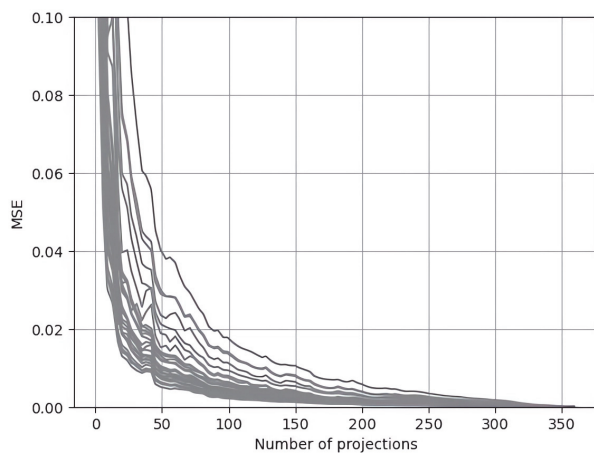

Fig. 3. Distribution of the reconstruction mean squared error from the number of measured projections for 25 randomly selected objects from the Low Doce CT Grand Challenge dataset

The paper [1] explores the notion of the CT scanning procedure as an anytime/anydose algorithm. An anytime algorithm is one capable of being terminated at any point, yielding an approximate result whose precision correlates with the number of calculations executed. Such algorithms find application in support systems and computer vision, where they facilitate a trade-off between quality and the time expended to attain that quality. In contrast, an anydose algorithm shares similarities with anytime algorithms but halts at a specified X-ray dose applied to the object.

Consider a scenario where the physical properties of the X-ray tomograph remain constant throughout the measurement process. These properties include detector resolution, X-ray tube voltage, and the object being measured, among others. The object being measured in this physical experiment is denoted as $\theta \in \Theta$. During the measurement protocol, we observe a set of projections $X = (X_1, X_2, \ldots)$ obtained through the X-ray detector.

The algorithm involves iteratively measuring projections. Let $(x_1, x_2, \ldots, x_n)$ denote a subset of n measured projections at the n-th step of the anytime algorithm. The resulting reconstruction from these n projections is denoted as $R_n(x_1, x_2, \ldots, x_n)$. Examples of partial reconstructions can be found in Fig. 1. The

primary concept behind the monitored reconstruction algorithm is to determine the optimal point to stop collecting new projections, considering the trade-off between the cost of measuring new projections and the improvement in reconstruction quality. The cost of the projection may refer to both the measurement time and the X-ray dose transmitted to the object.

Formally, the objective of the monitored algorithm is to minimize the loss function for partial reconstruction:

$$L_n(x_1,...,x_n) = \varepsilon(R_n(x_1,...,x_n),\theta) + c_n(x_1,...,x_n). \quad (1)$$

Here, L_n represents the loss function for the n-th partial reconstruction, R_n denotes the reconstruction at step n, $\varepsilon(R_n(x_1, x_2, \ldots, x_n), \theta)$ is a function that quantifies the error between the partial reconstruction and the known object θ, and $c_n(x_1, x_2, \ldots, x_n)$ is the cost function associated with the measured subset of projections $(x_1, \ldots, x_n)$. The cost function can be defined, for example, in terms of measurement time or the amount of X-ray dose absorbed by the object. The paper discusses the properties of the loss function and proposes a reconstruction error function that facilitates early stopping. Multiple stopping rules are introduced to minimize the loss function at each step. In this paper, the adopted early stopping rule is defined as:

$$\| R_{n-1} - R_n \|_2 < c, \quad (2)$$

where c denotes a predetermined constant that quantifies the cost of measuring projection. The cost for the nth reconstruction is expressed as $c_n = c \cdot n$. Furthermore, we define the error of the nth reconstruction, $\varepsilon(R_n, \theta)$, as the Euclidean distance between R_n and the optimal reconstruction R_T: $\varepsilon(R_n, \theta) = \|R_n - R_T\|_2$. This study explores various strategies for ordering the corners that are to be assembled. For the purposes of this paper, we will assume that the projections from the entire set of possible projections are assembled at random angles, without loss of generality. The approach is implemented as an anytime algorithm, which is detailed in the pseudo-code provided in Algorithm 1.

1: **Input:** A set of projections that can be measured **X**, projection cost c, reconstruction algorithm **A**

2:Output: Partial reconstruction $R_n(x_1, x_2, \ldots, x_n)$
3: Initialize $n \leftarrow 1$
4: Collect initial subset of projections (x_1) from **X**
5: $R_1 \leftarrow$ Perform initial partial reconstruction
6: **while** stopping criterion not met **do**
7: $n \leftarrow n + 1$
8: Measure new projection x_n from **X**
9: $R_n \leftarrow$ Perform partial reconstruction from $\mathbf{A}(x_1, x_2, \ldots, x_n)$
10: **if** $\|R_n - R_T\|_2 < c$ **then**
11: **Break**　　　　▶ Early stopping condition
12: **end if**
13: **if** $(x_1, \ldots, x_n)$ contains all elements from **X then**
14: **Break**
15: **end if**
16: **end while**

17: **Return** $R_n(x_1, x_2, \ldots, x_n)$

2. Anytime modeling

In this paper, simulated projections will be calculated using the Radon transform. As phantoms, full-dose reconstructions from the publicly available Low Dose CT Grand Challenge dataset [2, 23, 24, 25] will be utilized. The images in this dataset have dimensions of 512 by 512 pixels, and it comprises approximately 16 000 human reconstruction images, including the torso, thorax, and human head CT reconstruction images. For experimental setup, 75 % of the images from this dataset will be allocated for neural network training, 100 images for the test dataset for testing anytime algorithm with or without neural networks, and the remaining images for the validation dataset for neural networks.
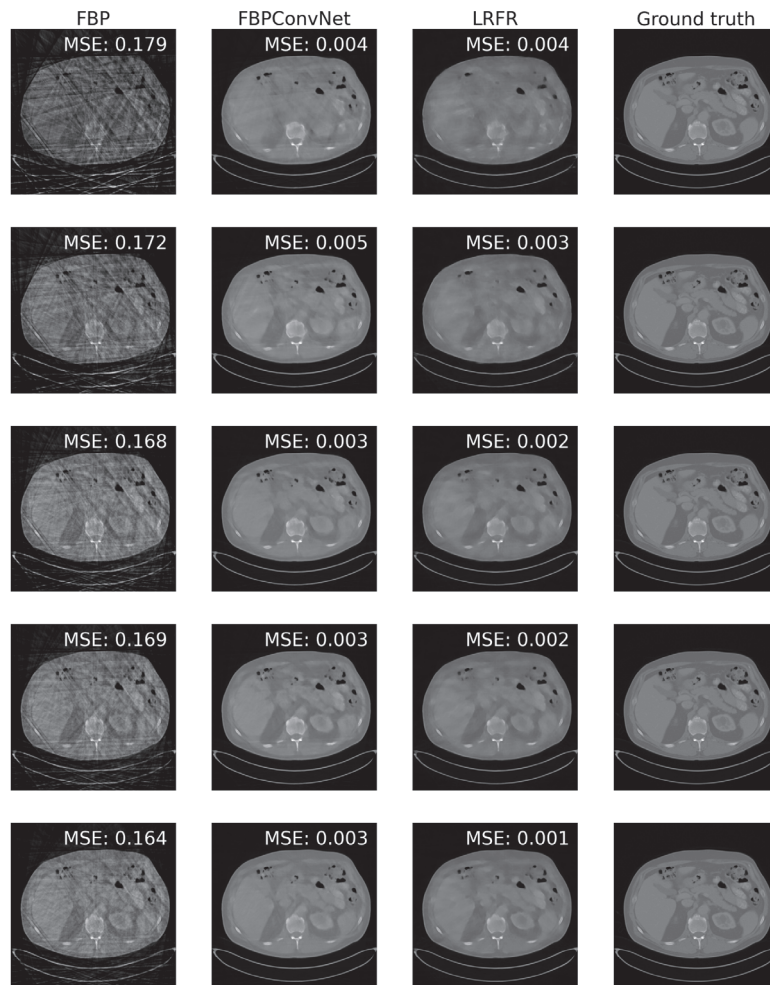

Fig. 4. Anytime algorithm

The space of all possible projections will be defined as a set of 360 projections spread across an angular range from 0 to 180 degrees. Within each iteration of the anytime algorithm, the projections will be ordered in a randomly determined order that remains constant throughout different partial reconstructions at the same step. Therefore, two distinct partial reconstructions at the same step of the anytime algorithm will be built from sets of projections measured at identical angles.

To calculate the projections, the Radon transform was applied to a two-dimensional phantom. The Radon transform was used from the ASTRA Toolbox library [26]. A parallel beam scheme was used with 768 detector cells, and the 'cuda' version of the Radon transform. The

size of the detector cell and the ideal image pixel were equivalent.

Additionally, the noise was modeled on the values after the radon transform. The projection values a_i obtained after the Radon transformation was used to generate a random variable using the following formula: $a_{i'} = a_i + a_i * normal(0, s)$, where $a_{i'}$ is the resulting projection values, $normal(0, s)$ – a random variable distributed according to the normal distribution with standard deviation s. In the framework of this work, the value $s = 0.001$ was used.

3. Neural network monitored reconstruction

Neural networks have exhibited impressive success in various image-processing tasks, including image reconstruction. In the field of CT imaging, neural network-based reconstruction algorithms offer the potential to surpass the limitations of traditional methods, delivering superior performance in terms of speed and quality.

Neural network methods for tomographic reconstruction are mainly built on two approaches. In the first approach, a neural network takes a set of measured projections as input and outputs a reconstruction (neural network reconstructors). In the second approach, the neural network takes as input a reconstruction image obtained by the classical method and improves it. This paper covers only the networks of the second approach, which were trained in the original works to improve the FBP reconstruction result. Two neural networks will be examined: FBPConvNet [28] and LRFR [29].

The first neural network, FBPConvNet, is a U-Net [28] applied to the few-view tomography problem. Mathematically, the operation of the neural network can be described as follows:

$$R_{n'} = R_n + NN(R_n). \tag{3}$$

Here, R_n represents the improved reconstruction, and $NN()$ denotes the function describing the transformation of the input image by the neural network. FBPConvNet takes a few-view reconstruction as input and calculates an additive component based on it, thereby enhancing the accuracy of the reconstruction. While this algorithm has demonstrated significant improvements in the accuracy of the few-view reconstruction, it has also exhibited instability when faced with changing angles or noise [30]. Nevertheless, FBPConvNet serves as a prominent benchmark for comparison in neural network-based tomographic reconstruction studies [29, 30, 21].

LRFR [29] is an enhancement of the FBPConvNet algorithm. It proposes an interpolation method for missing projections in few-view tomography tasks. Additionally, without departing from the reconstruction image space, it introduces an adjustment that avoids distorting the values of the original projections residing in the zero space of the Radon transform. This possibility is based on the central section theorem, which states that the frequency space of the reconstruction image contains the Fourier values of the projection image. The proposed algorithm has exhibited significant improvements in reconstruction accuracy while also increasing noise resilience.

This paper focuses solely on post-processing algorithms, considering the time required for training neural network algorithms. In both proposed approaches, the neural networks were trained on a fixed set of projection angles. However, anytime reconstruction involves performing reconstructions with a continually increasing number of angles. This work does not explore the generalization of the neural network post-processing model to a wide range of low-view reconstructions.

Consequently, the entire angular range of 360 angles was divided into 20 iterations of the anytime algorithm, with 18 projections collected for each new iteration. For each of these 20 iterations, a specific dataset of few-view reconstructions was prepared, and FBPConvNet and LRFR networks were trained on each dataset individually. Thus, a distinct neural network was utilized for each iteration of the anytime reconstruction, resulting in a total of 20 FBPConvNet networks and 20 LRFR networks being trained. These trained networks were used as reconstruction algorithms in the anytime algorithm (see Algorithm 1).

4. Results

To research the effectiveness of the reconstruction methods, we executed a range of experiments with varying projection measurement costs c, set between 10^{-2} and 10^{-4}. In these experiments, we fixed the cost c and conducted 100 anydose experiments. The outcomes, including the average number and standard deviation of measured projections, Mean Squared Error (MSE), Structural Similarity Index (SSIM), and the anydose loss function values, are summarized in Tab. 1 and 2.

The evaluation encompassed a comparison of the following algorithms: Filtered Back Projection (FBP), FBPConvNet, and Learned Residual Fourier Reconstruction (LRFR).

The data presented in the tables illustrate that the neural network-based algorithms (FBPConvNet and LRFR) exhibited enhanced reconstruction quality (by SSIM and MSE). This is further evidenced by the mean anytime loss metrics, which reflect the MSE of the reconstructions for each algorithm. Notably, the neural network algorithms demonstrated a marked improvement over the conventional FBP algorithm, as evidenced by their significantly reduced mean anytime losses, underscoring their superior performance in this context.

The analysis reveals that FBPConvNet exhibits the best results at higher projection costs. However, it is important to note that beyond a certain threshold of the number of steps in the anytime algorithm, the performance of FBPConvNet becomes less consistent. This is evident as the second norm of the disparity between individual FBPConvNet reconstructions

frequently surpasses the predetermined cost. As a result of this inconsistency, there is a significant increase in the reconstruction time when using FBPConvNet, in contrast to the more stable LRFR algorithm.

Tab. 1. Table of the results of simulated monitored reconstructions on 100 randomly selected test objects, where A represents FBP, B represents FBPConvNet, and C represents LRFR algorithms

c	Measured projection count			MSE			SSIM		
	A	B	C	A	B	C	A	B	C
$10^{-2.0}$	54±11	**36±0**	37±4	0.060	**0.006**	0.008	0.24	**0.65**	**0.65**
$10^{-2.2}$	63±11	**38±6**	43±12	0.052	**0.006**	0.007	0.26	0.66	**0.67**
$10^{-2.4}$	75±15	**44±13**	51±17	0.044	**0.005**	0.006	0.28	0.67	**0.68**
$10^{-2.6}$	86±18	**60±26**	63±17	0.036	**0.005**	**0.005**	0.30	0.68	**0.70**
$10^{-2.8}$	105±22	87±40	**78±18**	0.027	**0.004**	**0.004**	0.34	0.71	**0.71**
$10^{-3.0}$	127±28	133±53	**95±26**	0.021	**0.003**	0.004	0.37	**0.74**	0.72
$10^{-3.2}$	155±38	187±65	**123±39**	0.016	**0.003**	**0.003**	0.40	**0.77**	0.74
$10^{-3.4}$	194±44	258±83	**164±54**	0.011	**0.002**	0.003	0.43	**0.80**	0.77
$10^{-3.6}$	237±48	327±64	**220±70**	0.008	**0.002**	**0.002**	0.45	**0.83**	0.80
$10^{-3.8}$	278±56	357±18	**281±67**	0.006	**0.002**	**0.002**	0.48	**0.84**	0.83
$10^{-4.0}$	**322±50**	360±0	331±51	0.005	**0.002**	**0.002**	0.49	0.84	**0.86**

Tab. 2. Table of Loss values from the table 1, where A represents FBP, B represents FBPConvNet, and C represents LRFR algorithms

c	Loss		
	A	B	C
$10^{-2.0}$	0.090	**0.026**	0.029
$10^{-2.2}$	0.074	**0.019**	0.022
$10^{-2.4}$	0.060	**0.015**	0.017
$10^{-2.6}$	0.048	**0.013**	0.014
$10^{-2.8}$	0.036	0.012	**0.011**
$10^{-3.0}$	0.028	0.011	**0.009**
$10^{-3.2}$	0.021	0.009	**0.008**
$10^{-3.4}$	0.016	0.008	**0.006**
$10^{-3.6}$	0.012	0.006	**0.005**
$10^{-3.8}$	0.009	0.005	**0.004**
$10^{-4.0}$	0.006	0.004	**0.003**

This observation is critical as it highlights a trade-off between initial performance and long-term stability. While FBPConvNet shows promising results at the outset, particularly at higher projection costs, its tendency to exceed the set cost in prolonged processing phases leads to increased computational time. In contrast, LRFR maintains a more consistent performance, avoiding dramatic escalations in measurement time and dose.

In our analysis, Fig. 7, 8 offer detailed insights. In Fig. 7, each point represents the number of projections used during the anytime experiment against the corresponding final reconstruction error. These figures demonstrate that neural network models consistently outperformed the FBP algorithm in accuracy across all experiments. However, it's important to note that many experiments using FBPConvNet produced less optimal results, as indicated by the scattered points on the plots. This dispersion suggests instability in reconstructions using FBPConvNet meshes, highlighting challenges in dealing with constantly changing reconstructions. These less successful trials did not significantly enhance overall accuracy, as shown in the figures .

Neural networks were trained using the following parameters: AdamW optimizer, batch size of 2, gradient vector normalization of 1, and learning rate of 1e-3 for FBPConvNet and 1e-4 for LRFR. The training process employed the early stopping rule, which halted training if the validation loss function did not improve for three consecutive epochs. Each epoch consisted of approximately 8800 batches. To mitigate strong overfitting, few-view reconstructions, and projection noise were generated dynamically during training.

FBPConvNet networks were trained for 5 to 9 epochs, while LRFR training required 3 to 4 epochs for convergence.

The training was conducted on a computer equipped with two Nvidia video cards: Titan Xp and GTX 1080. The distributed data-parallel algorithm implemented in the PyTorch Lightning [27] library was utilized to distribute a batch of 2 images between the two video cards. The training time per epoch ranged from 30 to 60 minutes for FBPConvNet and from 40 minutes to 150 minutes for LRFR.

Fig. 5 showcases examples of partial reconstructions obtained from the same projections using both the FBP algorithm and the trained neural networks. The figure clearly illustrates that the neural network reconstruction algorithms closely approach the ideal reconstruction image. In this paper, the specific values of the reconstruction quality metrics for each of the 40 neural networks are not provided, as the cumulative effect will be evident within the context of anytime reconstruction with a neural network.

Once all neural networks were trained, they were employed as reconstruction algorithms for the respective stages of anytime reconstruction. Fig. 6 illustrates the mean squared error (MSE) reconstruction errors for the partial reconstructions of four different objects from the test dataset. The results clearly demonstrate that the accuracy of neural network reconstruction surpasses that of classical algorithms by approximately an order of magnitude. However, it should be noted that neural network anytime algorithms no longer exhibit monotonic convergence of MSE.
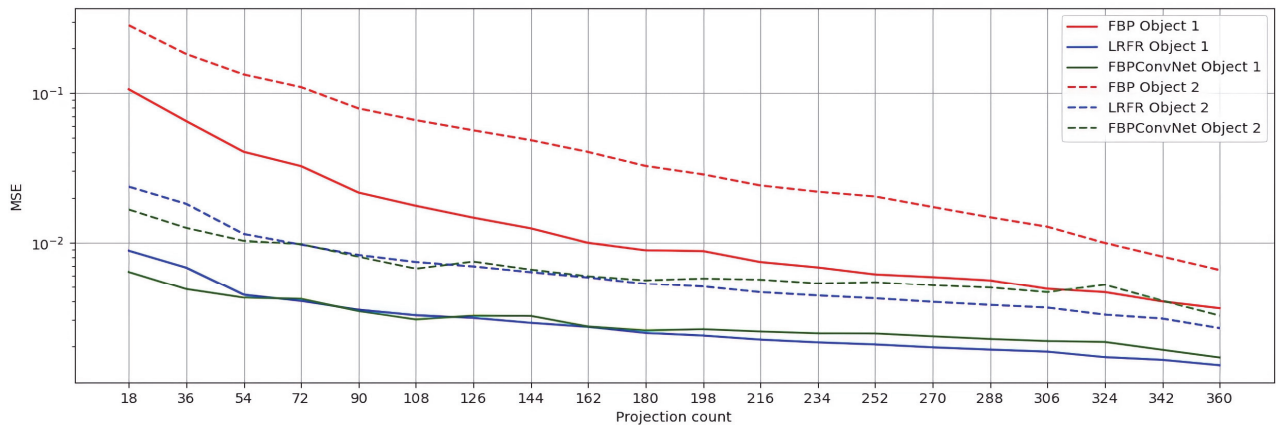
Fig. 5. Partial reconstructions generated using different projection counts by the FBP, FBPConvNet, and LRFR reconstruction algorithms

To provide a detailed analysis of the obtained results, Fig. 7, 8 have been included for $c = 0.5*10^{-3}$. These figures present a multitude of data points, each offering insights into the reconstructions carried out at different stages. In Fig. 7, each point corresponds to the number of projections taken during a specific time interval of the experiment, along with the final reconstruction error. Fig. 8, on the other hand, displays each point as the ratio of the number of received projections to the value of the anytime loss function, as defined in formula (1). As can be observed, a significant number of FBPConvNet breakpoints are located near the maximum allowed number of projections (360 projections), which again shows the instability of the results of this network for low projection cost values. And as can be seen from the figures, such failed experiments did not lead to a significant increase in accuracy.

5. Discussion

The present study employed an approach that, upon reflection, can be considered inefficient due to the requirement of training a separate neural network for each fixed set of projection angles. This approach not only demands substantial computational resources for training but also restricts the flexibility to modify the selected sequence of angles in the anytime algorithm after training. It is important to acknowledge that there can be existing or more efficient neural approaches that can achieve high-quality reconstructions with any projection angles set using a single neural network.

For instance, postprocessing neural networks, such as FBPConvNet, offer a viable alternative that only necessitates a change in the training methodology. Additionally, other approaches, such as equally distributed sequences of projection angles or selecting angles based on their information content, were not explored in this study. These alternative approaches could serve as a tangential extension to the current research, offering potential avenues for further exploration and development.
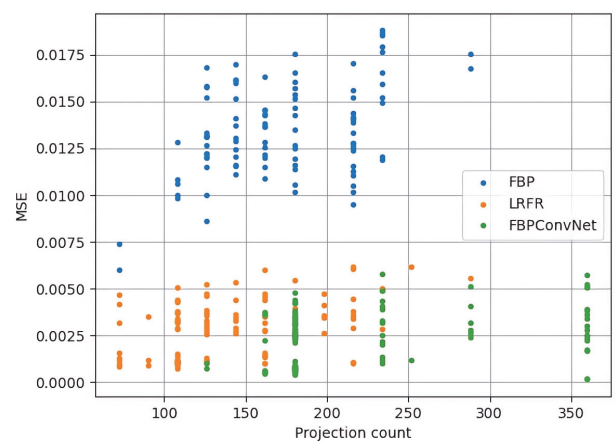

Fig. 6. Mean squared errors of partial reconstruction provided by FBP, LRFR, FBPConvNet with different projection count
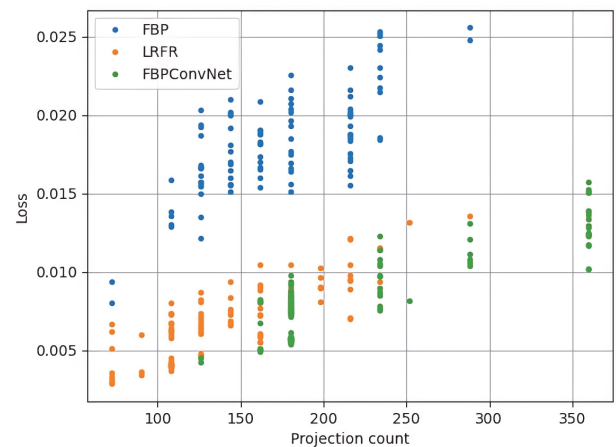

Fig. 7. Point cloud showing the result of anytime reconstructions with c = 0.5*10⁻³ for 100 different objects using the FBP, FBPConvNet, LRFR reconstruction algorithms. The position of each point describes the number of measured projections up to the mean squared error of final reconstruction

Conclusion

This paper addressed the problem of enhancing the anytime reconstruction method using neural network models. The findings demonstrated that neural network algorithms can significantly improve the accuracy of reconstructions by nearly an order of magnitude, while

also moderately reducing the number of projections necessary for the reconstruction process. However, it is important to note that not all neural network algorithms are suitable for integration into the anytime reconstruction framework. Specifically, weakly robust algorithms like FBPConvNet may inadvertently lead to an increase in X-ray dose, despite the advancements in reconstruction accuracy.

Acknowledgements

References

[1] Bulatov K, Chukalina M, Buzmakov A, Nikolaev D, Arlazarov V. Monitored reconstruction: Computed tomography as an anytime algorithm. IEEE Access 2020; 8: 110759-110774. DOI: 10.1109/ACCESS.2020.3002019.

[2] McCollough C. TU-FG-207A-04: Overview of the low dose CT grand challenge. Med Phys 2016; 43: 3759-3760. DOI: 10.1118/1.4957556.

[3] Yu W, Zeng L. A novel weighted total difference based image reconstruction algorithm for few-view computed tomography. PLoS One 2014; 9: e109345. DOI: 10.1371/journal.pone.0109345.

[4] Hanson K, Wecksung G. Bayesian approach to limited-angle reconstruction in computed tomography. J Opt Soc Am 1983; 73(11): 1501-1509. DOI: 10.1364/JOSA.73.001501.

[5] Nguyen, L. How strong are streak artifacts in limited angle computed tomography? Inverse Probl 2015; 31(5): 055003. DOI: 10.1088/0266-5611/31/5/055003.

[6] Yu W, Wang C, Huang M. Edge-preserving reconstruction from sparse projections of limited-angle computed tomography using l 0-regularized gradient prior. Rev Sci Instrum 2017; 88: 043703 DOI: 10.1063/1.4981132.

[7] Marshall H, Bowman R, Yang I, Fong K, Berg C. Screening for lung cancer with low-dose computed tomography: a review of current status. J Thorac Dis 2013; 5: S524. DOI: 10.3978/j.issn.2072-1439.2013.09.06.

[8] Wenholz A, Okereke I. Lung cancer screening using low-dose computed tomography. In Book: El-Baz A, Suri J, eds. Lung imaging and CADx. Ch 5. Boca Raton: CRC Press; 2019. DOI: 10.1201/9780429055959-5.

[9] Leuschner J, Schmidt M, Baguer D, Maass P. LoDoPaB-CT, a benchmark dataset for low-dose computed tomography reconstruction. Sci Data 2021; 8, 109. DOI: 10.1038/s41597-021-00893-z.

[10] Smith-Bindman R, et al. Is computed tomography safe? N Engl J Med 2010; 363: 1-4. DOI: 10.1056/NEJMp1002530.

[11] Giantsoudi D, De Man B, Verburg J, Trofimov A, Jin Y, Wang G, Gjesteby L, Paganetti H. Metal artifacts in computed tomography for radiation therapy planning: dosimetric effects and impact of metal artifact reduction. Phys Med Biol 2017; 62: R49. DOI: 10.1088/1361-6560/aa5293.

[12] Shikhaliev P. Beam hardening artefacts in computed tomography with photon counting, charge integrating and energy weighting detectors: a simulation study. Phys Med Biol 2005; 50: 5813. DOI: 10.1088/0031-9155/50/24/004.

[13] Joseph P, Spital R. The effects of scatter in X-ray computed tomography. Med Phys 1982; 9: 464-472. DOI: 10.1118/1.595111.

[14] Chen G, Kung J, Beaudette K. Artifacts in computed tomography scanning of moving objects. Semin Radiat Oncol 2004; 14: 19-26. DOI: 10.1053/j.semradonc.2003.10.004.

[15] Tian C, Fei L, Zheng W, Xu Y, Zuo W, Lin C. Deep learning on image denoising: An overview. arXiv Preview. 2020. Source: <https://arxiv.org/abs/1912.13171>. DOI: 10.48550/arXiv.1912.13171.

[16] Kappeler A, Yoo S, Dai Q, Katsaggelos A. Video super-resolution with convolutional neural networks. IEEE Trans Comput Imaging 2016; 2: 109-122. DOI: 10.1109/TCI.2016.2532323.

[17] Xie J, Xu L, Chen E. Image denoising and inpainting with deep neural networks. Proc 25th Int Conf on Neural Information Processing Systems (NIPS'12) 2012; 1: 341-349.

[18] Hu D, Zhang Y, Quan G, Xiang J, Coatrieux G, Luo S, Coatrieux J, Ji X, Han H, Chen Y. CROSS: Cross-domain residual-optimization based structure strengthening reconstruction for limited-angle CT. IEEE Trans Radiat Plasma Med Sci 2023; 7(5): 521-531. DOI: 10.1109/TRPMS.2023.3242662.

[19] Li Q, Li R, Li S, Wang T, Cheng Y, Zhang S, Wu W, Zhao J, Qiang Y, Wang L. Unpaired low-dose computed tomography image denoising using a progressive cyclical convolutional neural network. Med Phys 2023; 51(2): 1289-1312. DOI: 10.1002/mp.16331.

[20] Ma Y, Ren Y, Feng P, He P, Guo X, Wei B. Sinogram denoising via attention residual dense convolutional neural network for low-dose computed tomography. Nucl Sci Tech 2021; 32: 41. DOI: 10.1007/s41365-021-00874-2.

[21] Adler J, Öktem O. Learned primal-dual reconstruction. IEEE Trans Med Imaging 2018; 37: 1322-1332. DOI: 10.1109/TMI.2018.2799231.

[22] Ghadrdan S, Alirezaie J, Dillenseger J, Babyn P. Low-dose computed tomography image denoising based on joint wavelet and sparse representation. 36th Annual Int Conf of the IEEE Engineering In Medicine And Biology Society 2014: 3325-3328. DOI: 10.1109/EMBC.2014.6944334.

[23] Moen T, Chen B, Holmes III D, Duan X, Yu Z, Yu L, Leng S, Fletcher J, McCollough C. Low-dose CT image and projection dataset. Med Phys 2021; 48: 902-911. DOI: 10.1002/mp.14594.

[24] Clark K, Vendt B, Smith K, Freymann J, Kirby J, Koppel P, Moore S, Phillips S, Maffitt D, Pringle M, Tarbox L, Prior F. The Cancer Imaging Archive (TCIA): maintaining and operating a public information repository. J Digit Imaging 2013; 26: 1045-1057. DOI: 10.1007/s10278-013-9622-7.

[25] McCollough C, Chen B, Holmes D, Duan X, Yu Z, Xu L, Leng S, Fletcher J. Low dose CT image and projection data [data set]. The Cancer Imaging Archive 2020; 10. DOI: 10.1002/mp.14594.

[26] Van Aarle W, Palenstijn W, Cant J, Janssens E, Bleichrodt F, Dabravolski A, De Beenhouwer J, Batenburg K, Sijbers J. Fast and flexible X-ray tomography using the ASTRA toolbox. Opt Express 2016; 24(22): 25129-25147. DOI: 10.1364/OE.24.025129.

[27] Falcon W. PyTorch lightning. GitHub. 3 (2019)

[28] Jin K, McCann M, Froustey E, Unser M. Deep convolutional neural network for inverse problems in imaging. IEEE Trans Image Process 2017; 26: 4509-4522. DOI: 10.1109/TIP.2017.2713099.

[29] Yamaev AV, Chukalina MV, Nikolaev DP, Kochiev LG, Chulichkov AI. Neural network regularization in the

problem of few-view computed tomography. Computer Optics 2022; 46(3): 422-428. DOI: 10.18287/2412-6179-CO-1035.

[30] Smolin A, Yamaev A, Ingacheva A, Shevtsova T, Polevoy D, Chukalina M, Nikolaev D, Arlazarov V. Reprojection-based numerical measure of robustness for CT reconstruction neural network algorithms. Mathematics 2022; 10: 4210. DOI: 10.3390/math10224210.

[31] Pan X, Sidky E, Vannier M. Why do commercial CT scanners still employ traditional, filtered back-projection for image reconstruction? Inverse Problems 2009; 25: 123009. DOI: 10.1088/0266-5611/25/12/123009.

Author's information

Andrei Viktorovich Yamaev, (b. 1996) is PhD student in Moscow State University from 2018. Currently he works as the researcher at the "Smart Engine Service Ltd" company. Research interests are neural networks, computed tomography, programming. E-mail: *rewin1996@gmail.com*